PAPER

Structural features associated with multiferroic behavior in the $RX_3(BO_3)_4$ system

Structural features associated with multiferroic behavior in the $RX_3(BO_3)_4$ system

H Zhang[1], S Liu[1], C S Nelson[2], L N Bezmaternykh[3], Y-S Chen[4], S G Wang[4], R P S M Lobo[5,6], K Page[7], M Matsuda[7], D M Pajerowski[7], T J Williams[7] and T A Tyson[1,8]

[1] Department of Physics, New Jersey Institute of Technology, Newark, NJ 071022, United States of America
[2] National Synchrotron Light Source II, Brookhaven National Laboratory, Upton, NY 11973, United States of America
[3] L.V. Kirensky Institute of Physics, Krasnoyarsk, Russia
[4] Center for Advanced Radiation Sources, University of Chicago, Argonne, Chicago, IL 60439, United States of America
[5] Laboratoire de Physique et d'Etude des Materiaux (LPEM), ESPCI Paris, PSL University, CNRS, 75005 Paris, France
[6] Sorbonne Université, CNRS, LPEM. 75005 Paris, France
[7] Neutron Scattering Division, Oak Ridge National Laboratory, Oak Ridge, TN 37831, United States of America

E-mail: tyson@njit.edu (T A Tyson)

CrossMark

Abstract
The magnetoelectric effect in the $RX_3(BO_3)_4$ system (R = Ho, Eu, Sm, Nd, Gd; X = Fe, Al) varies significantly with the cation R despite very similar structural arrangements. Our structural studies reveal a symmetry reducing tilting of the BO_3 planes and of the FeO_6 polyhedra in the systems exhibiting low magnetic field induced electric polarization. Neutron scattering measurements reveal a lack of magnetic ordering indicating the primary importance of the atomic structure in the multiferroic behavior of this system.

Keywords: multiferroic, magnetoelectric, crystal structure, ferroelectric, spin-lattice coupling

S Supplementary material for this article is available online

(Some figures may appear in colour only in the online journal)

1. Introduction

In multiferroic materials both magnetic and electronic long-range order coexist with different coupling magnitudes between them [1–5]. Strongly coupled materials are particularly interesting for new sensors and data storage devices with novel features, such as the low energy cost for writing information (polarization bits) with electric fields and reading with magnetic field sensors. In the most studied multiferroic system $BiFeO_3$, [6] the coexisting magnetic and ferroelectric order parameters are weakly coupled, limiting the range of applications. The development and study of new classes of materials with large magnetoelectric couplings is of utmost interest.

In the search for materials with large magnetoelectric couplings, the $RX_3(BO_3)_4$ (R = rare earth, X = Fe, Al) class has attracted considerable attention in recent years due to its large magnetoelectric effect [7–12]. In the case of R = Ho and X = Al, the system remains in a stable hexagonal phase of space group R32 down to low temperatures, and the electric polarization can be as large as 0.36 μC cm^{-2} [13] for finite magnetic fields. Previous studies suggested an enhanced structural correlation between the neighboring HoO_6 polyhedra and the possibility of local ordering of Ho magnetic sites ordering at low temperature [14]. On the other hand, the magnetic field induced polarization in the Fe based system

[8] Author to whom any correspondence should be addressed.

$RFe_3(BO_3)_4$ (R = Ho, Eu, Sm, Nd, Gd) has significantly smaller values (below 0.05 μC cm^{-2}) [15–19]. The largest values for this system are for R = Sm (P ~ 0.05 μC cm^{-2} at 5 K) [17] and R = Nd (P ~ 0.04 μC cm^{-2} at 5 K) [19].

The complex magnetic structure in the full class of the X = Fe system is an interesting path towards a stronger magnetoelectric coupling. In particular the iron borates $RFe_3(BO_3)_4$ with R = Ho, Tb, Gd and Eu show a first-order structural phase transition from R32 to $P3_121$ [20]. In addition, the $RFe_3(BO_3)_4$ system exhibit a complex magnetic structure due to the presence of open R (4f) and Fe (3d) atomic shells. A first magnetic transition (due to Fe and/or R site ordering [21]) occurs near ~40 K. In the case of R = Ho and Gd, a strong coupling between spins on the R and Fe sites lead to an additional spin reorientation of the Fe moments in the *a-b* plane at lower temperatures (~10 K for Gd and ~5 K for Ho) [22–27]. In this system, the materials which possess the highest electric field induced polarization are the ones that are stable in the R32 space group at low temperatures, such as in R = Sm and Nd.

To find the critical structural features the associated with the magnetoelectric effect in the broader $RX_3(BO_3)_4$ class, we conducted a systematic temperature dependent study of the structural properties on multiple length scales. High-resolution single-crystal synchrotron x-ray diffraction experiments have been carried out for R = Ho, Eu Sm, Nd, Gd; X = Fe, and for the $HoAl_3(BO_3)_4$ system, to probe the structural changes between 10 K and 300 K. In addition, powder and single-crystal neutron diffraction measurements have been conducted for $HoAl_3(BO_3)_4$ (HABO) to search for possible Ho site ordering at low temperature. The structural studies reveal a symmetry reducing tilting of the BO_3 planes and tilting of the FeO_6 polyhedra in the systems exhibiting very low magnetic field induced electric polarization.

2. Experimental details

$RX_3(BO_3)_4$ (R = Ho, Eu, Sm, Nd, Gd; X = Fe, Al) single crystals were grown from solution–melts based on bismuth trimolybdate and lithium molybdate. The preparation details can be found in [28]. Detailed x-ray characterization of the $HoAl_3(BO_3)_4$ system can be found in [29].

Heat capacity measurements on $HoAl_3(BO_3)_4$ single crystals were carried out with a Physical Property Measurement System (PPMS, Quantum Design) on warming and cooling between 2 K and 300 K to locate transitions and determine their nature, utilizing a relaxation method [30]. Addenda measurements (grease without sample) were collected and subtracted from the sample measurements. The heat capacity data were fitted with a double Debye model above the magnetic transitions (see [29]):

$$C_p = 9qNk \left[\nu \left(\frac{T}{\theta_{D1}} \right)^3 \int_0^{\theta_{D1}/T} \frac{x^4 e^x}{(e^x - 1)^2} dx \right.$$
$$\left. + (1 - \nu) \left(\frac{T}{\theta_{D2}} \right)^3 \int_0^{\theta_{D2}/T} \frac{x^4 e^x}{(e^x - 1)^2} dx \right]. \quad (1)$$
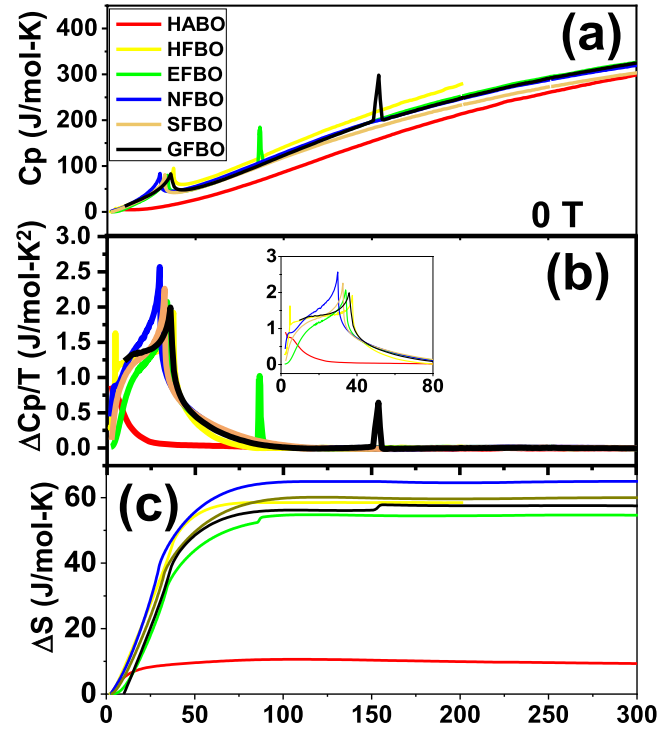

Figure 1. (a) Heat capacity measurements for R = Ho, Eu, Nd, Sm, Gd and A = Al, Fe. (b) C_p/T for the same systems measured. The inset shows the expanded region between 0 and 80 K. (c) Change of the entropy (magnetic) for different samples.
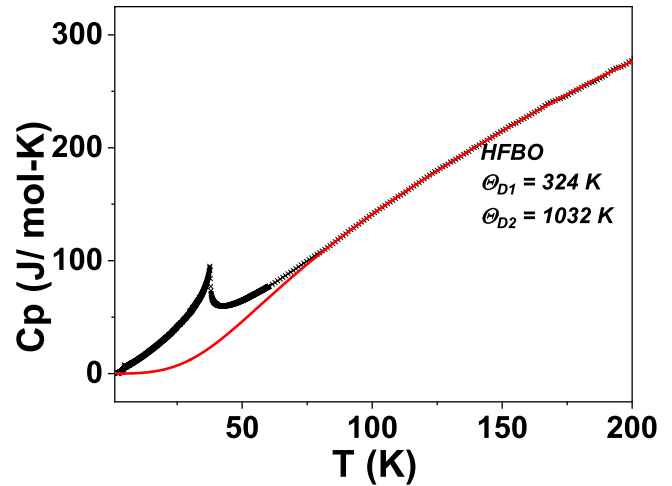

Figure 2. Results of the heat capacity measurements fit with a double Debye model of HFBO. The black circles are data taken from the measurements and the red curves are from equation (1) in the text.

Single-crystal x-ray diffraction measurements were performed at beamline 15-ID-D at the Advanced Photon Source (APS) at Argonne National Laboratory (ANL). The samples measured were single-phase crystals with ~20 μm diameter. A monochromatic focused beam of wavelength 0.413 28 Å and size 100 μm × 100 μm was used. Data were collected with a PILATUS 1M detector between 10 K to 300 K (for systems HABO, EFBO, SFBO, GFBO) and between 10 K to 70 K (HFBO and NFBO). For HFBO and NFBO, the data between 100 K and 300 K were collected with a CCD detector. The
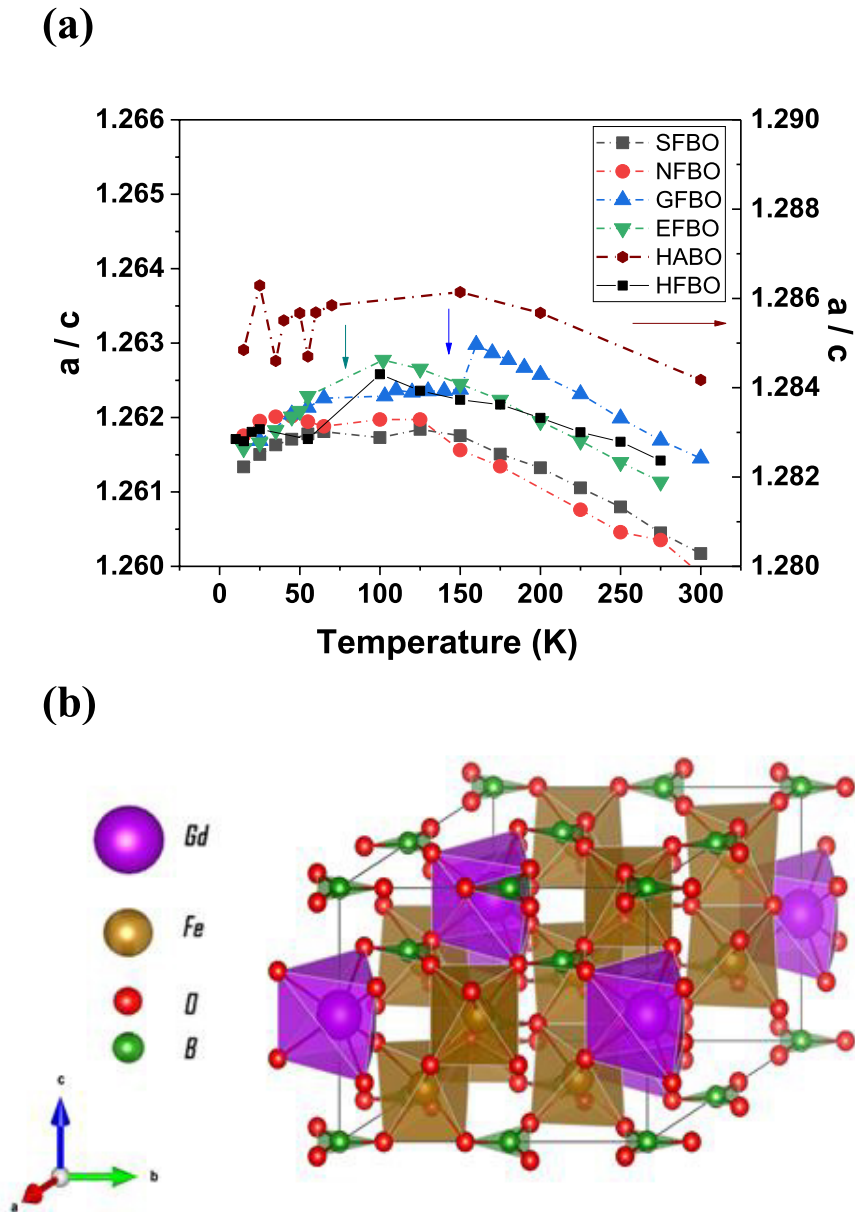
(a)

(b)

Figure 3. (a) The *a/c* ratio versus temperature from the single crystal XRD refinements. Note that the right-hand ordinate refers to HABO, and the left-hand ordinate to all other systems. (b) The unit cell of GdFe$_3$(BO$_3$)$_4$ at 300 K (P3$_1$21).

images were processed with APEX II and APEX III Bruker software for data reduction and with SADABS [31] for absorption corrections. Data reduction and structure solutions were conducted with XPREP [32] and SHELXT [33]. Full space group checks were conducted with PLATON [34].

To explore possible magnetic ordering, powder neutron diffraction experiments were performed on HoAl$_3$(BO$_3$)$_4$ at station Nanoscale-ordered Materials Diffractometer (NOMAD) at the Spallation Neutron Source (SNS), Oak Ridge National Laboratory (ORNL), and HB-1 at high flux isotope reactor (HFIR), ORNL. Single-crystal neutron diffractions between 5 K and 300 K were conducted at beamline HB-1 at HFIR at ORNL. For the single crystal measurements, a beam of wavelength 2.46 Å was used. The sample was aligned before the measurement with the *c* axis in the horizontal plane. The

data were collected in a specific region of reciprocal space to search for the forbidden peaks (100) and (101), together with the reference peaks (202) and (003). The exposure time for (100) and (101) peaks was 90 s at each temperature, and 15 s for the intense (202) and (003) peaks. The software package GRAFFITI was used for data analysis.

3. Results and discussions

HoFe$_3$(BO$_3$)$_4$ (HFBO), GdFe$_3$(BO$_3$)$_4$ (GFBO) and EuFe$_3$(BO$_3$)$_4$ (EFBO) exhibit a structural phase transition at ~420 K, 156 K, and 88 K, respectively [20]. This agrees well with our heat capacity measurements, shown in figure 1, where the sharp peaks near 156 K and 88 K signal the

Table 1. Structural parameters from $GdFe_3(BO_3)_4$ at 300 K.

Atoms	X	y	Z	U_{eq} (Å^2)	
Gd	0.0000	0.0000	0.5000	0.007 22(9)	
Fe	0.116 73(7)	0.3333	0.8333	0.005 21	
O1	0.1874(3)	0.2129(3)	0.6825(3)	0.0081(3)	
O2	0.0000	0.4084(4)	1.0000	0.0124(7)	
O3	0.0000	0.1438(3)	1.0000	0.0070(4)	
B1	0.0000	0.5530(4)	1.0000	0.0062(5)	
B2	0.0000	0.0000	1.0000	0.0057(8)	
U_{ij}(Gd) 0.007 52(10)	0.007 52(10)	0.006 62(13)	0.000	0.000	0.003 76(5)
U_{ij}(Fe) 0.004 97(19)	0.0050(2)	0.0057(3)	−0.000 15(13)	−0.000 08(6)	0.002 52(10)
U_{ij}(O1) 0.0077(7)	0.0102(8)	0.0081(8)	−0.0017(7)	−0.0002(6)	0.0057(6)
U_{ij}(O2) 0.0141(13)	0.0081(10)	0.0170(17)	0.0041(6)	0.0083(13)	0.0070(6)
U_{ij}(O3) 0.0082(11)	0.0052(7)	0.0086(11)	0.0008(4)	0.0017(8)	0.0041(5)
U_{ij}(B1) 0.0070(17)	0.0055(10)	0.0067(12)	0.0005(6)	0.0010(12)	0.0035(8)
U_{ij}(B2) 0.0061(13)	0.0061(13)	0.005(2)	0.000	0.000	0.0030(6)

Space group: R32.
$a = 9.5526(4)$ Å.
$c = 7.5727(3)$ Å.
$D_x = 4.662$ g cm^{-3}.
Measurement temperature: 300 K.
Crystal diameter: ~20 μm.
Wavelength: 0.413 28 Å.
2θ range: 4.2°–40.2°.
Flack parameter: 1.04(4).
Absorption coefficient: 2.9 mm^{-1}.
EXTI extinction parameter: 0.014 81.
Number of unique observed reflections $F_o > 4\sigma(F_o)$: 639.
Number of fitting parameters: 36.
Amplitude of max peak in final difference map: 0.56 e Å^{-3} (Gd).
$R_1 = 1.3\%$, w$R_2 = 3.6\%$, goodness of fit = 0.4.
[a] Atomic displacement parameters U_{ij}(Å^3) are in the order U_{11}, U_{22}, U_{33}, U_{23}, U_{13}, U_{12}.

first-order structural phase transition in GFBO and EFBO, respectively and peaks near ~40 K indicate the magnetic ordering transitions involving the Fe ions. The magnetic transition temperature of the system with R = Ho is not within the measurement range. The heat capacity data were fitted with a double Debye to model (equation (1)) to account for the phonons and to extract the change in entropy (magnetic) below the structural phase transitions. IR reflectivity measurements were conducted at 300 K following the methods in [35], in order to determine the phonon modes of these materials. The reflectivity data for NFBO—shown in the supplementary material (figure A1 (available online at stacks.iop.org/JPhysCM/31/505704/mmedia))—gives an argument for the use of a double, instead of a simple, Debye model. Indeed, the infrared data indicate two separate groups of phonons at temperatures compatible with our fitting parameters. An example fit is shown in figure 2 for HFBO and the fits for all other samples are given in figure A2 of the supplementary document.

The extracted Debye temperature θ_{D1} (mainly contributed by the rare earth atom) in HABO ($\theta_{D1} = 535$ K) is the largest among all the system measured. This indicates a maximum stiffness in the iron containing borates series. Figure 1(c) shows the entropy from the low temperature transitions in all samples. The expected value due to magnetic ordering alone is $\Delta S = R \ln(2S + 1)$. Let us utilize R = Sm as an example: taking three iron atoms with spin S1 = 5/2 and

one Sm atom with spin S2 = 5/2 into consideration leads to $\Delta S = 59.6$ J K^{-1} which is within 3% of the results obtained from the heat capacity data and shown in figure 1(c). We observed the highest entropy jump in the system with R = Nd (S2 = 3/2). It also differs by ~13% from the calculated value, suggesting additional contributions to the specific heat of NFBO at low temperature.

The crystal structures were determined by synchrotron-based temperature-dependent single-crystal diffraction measurements. We found that the high-temperature phase of the HFBO, GFBO, and EFBO is R32 and the low-temperature structure is P3$_1$21. Meanwhile, all other systems—SmFe$_3$(BO$_3$)$_4$, NdFe$_3$(BO$_3$)$_4$ and HoAl$_3$(BO$_3$)$_4$—remain in the R32 space group between 10 K and 300 K. Tables 1 and 2 shows the refinement results for GdFe$_3$(BO$_3$)$_4$ at 300 K and 110 K, respectively. The structure determination for other systems is done in the same way. Detailed refinement results for all other systems (at the highest and the lowest measured temperatures) can be found in the supplementary document.

Figure 3(a) shows the lattice parameters ratio a/c extracted from the refinements. Note the right y-axis scale is for the HABO system only and the left y-axis scale is for the iron borate systems. The a/c ratio for HABO is much larger than any of the iron-based systems, indicating that the former is more closely packed in the c direction [29]. Meanwhile, the phase transitions in the GFBO and EFBO (indicated as vertical arrows in figure 3(a)) appear as jumps (vertical arrows) in the

Table 2. Structural parameters from $GdFe_3(BO_3)_4$ at 110 K.

Atoms	X	y	Z	U_{eq} (Å²)	
Gd	0.666 63(2)	0.666 63(2)	1.0000	0.003 08(9)	
Fe1	1.0000	0.884 77(9)	0.6667	0.002 73(14)	
Fe2	0.335 57(5)	0.549 88(9)	0.325 30(5)	0.002 83(13)	
O1	0.8123(4)	0.8123(4)	0.5000	0.0046(6)	
O2	0.5244(4)	0.6697(2)	0.4933(2)	0.0050(5)	
O3	1.0780(4)	1.0780(4)	0.5000	0.0065(6)	
O4	0.2703(3)	0.6868(3)	0.4723(3)	0.0058(4)	
O5	0.8808(3)	0.6957(3)	0.8198(3)	0.0049(4)	
O6	0.2158(3)	0.3624(3)	0.4817(3)	0.0044(4)	
O7	0.4614(3)	0.4766(4)	0.1853(4)	0.0045(4)	
B1	0.6679(4)	0.6679(4)	0.5000	0.0028(9)	
B2	0.4472(5)	0.3274(4)	0.1767(4)	0.0034(6)	
B3	1.2219(6)	1.2219(6)	0.5000	0.0038(7)	
U_{ij}(Gd) 0.003 21(11)	0.003 21(11)	0.002 91(12)	0.000 08(2)	−0.000 08(2)	0.001 68(7)
U_{ij}(Fe1)0.0029(3)	0.0027(2)	0.0026(3)	0.000 01(10)	0.000 03(19)	0.001 46(14)
U_{ij}(Fe2)0.0030(2)	0.0027(2)	0.0028(2)	0.000 11(11)	−0.000 01(15)	0.001 34(15)
U_{ij}(O1) 0.0042(10)	0.0042(10)	0.0038(13)	0.0009(5)	−0.0009(5)	0.0010(12)
U_{ij}(O2) 0.0040(10)	0.0061(13)	0.0048(11)	−0.0018(9)	−0.0006(7)	0.0023(8)
U_{ij}(O3) 0.0057(10)	0.0057(10)	0.0067(12)	0.0011(5)	−0.0011(5)	0.0018(11)
U_{ij}(O4) 0.0051(9)	0.0069(9)	0.0062(7)	−0.0021(7)	−0.0019(7)	0.0037(8)
U_{ij}(O5) 0.0062(11)	0.0041(10)	0.0044(9)	0.0009(7)	0.0006(8)	0.0025(8)
U_{ij}(O6) 0.0069(10)	0.0032(9)	0.0035(9)	0.0001(7)	0.0006(7)	0.0028(8)
U_{ij}(O7) 0.0056(10)	0.0041(10)	0.0053(9)	0.0002(7)	0.0007(8)	0.0036(8)
U_{ij}(B1) 0.0027(15)	0.0027(15)	0.002(2)	−0.0005(6)	0.0005(6)	0.0005(13)
U_{ij}(B2) 0.0041(13)	0.0029(16)	0.0035(12)	−0.0003(11)	−0.0001(9)	0.0019(11)
U_{ij}(B3) 0.0041(14)	0.0041(14)	0.0034(16)	0.0001(8)	−0.0001(8)	0.0023(17)

Space group: $P3_121$.

$a = 9.5454(4)$ Å $c = 7.5615(3)$ Å.

$D_x = 4.676$ g cm^{-3}.

Measurement temperature: 110 K.

Crystal diameter: ~20 μm.

Wavelength: 0.413 28 Å.

2θ range: 2.8°–40.2°.

Flack parameter: 1.10(4).

Absorption coefficient: 2.9 mm^{-1}.

EXTI extinction parameter: 0.012 43.

Number of unique observed reflections $F_o > 4\sigma(F_o)$: 1606.

Number of fitting parameters: 96.

Amplitude of max peak in final difference map: 0.67 e Å^{-3} (O2).

$R_1 = 1.9\%$, w$R_2 = 5.5\%$, goodness of fit $= 1.0$.

[a] Atomic displacement parameters U_{ij}(Å³) are in the order U_{11}, U_{22}, U_{33}, U_{23}, U_{13}, U_{12}.

trends of a/c versus temperature. (Note that the low temperature (<100 K) and higher temperature (>100 K) measurements for HABO and NFBO were done with different experimental setups and detectors (see experimental details) therefore the trends of these curves are not continuous.)

Below, we analyze in detail the change of the crystal structure with temperature. Figure 3(b) shows the structure of $GdFe_3(BO_3)_4$ at 300 K, indicating that the Gd and Fe atom both have six neighboring oxygen atoms. The top and bottom surfaces of the GdO_6 polyhedra (O_3 layers) are parallel to the ab plane, while in the FeO_6 polyhedra they are slightly tilted. The BO_3 triangles which connect the GdO_6 and FeO_6 polyhedra are also parallel to the ab plane. Table 1 contains the full refinement results.

Table 2 shows that, when the system is cooled below the structural transition at 156 K, half of the FeO_6 polyhedra become distorted and the interconnecting BO_3 planes tilt with respect to the ab plane of the unit cell. The displacements of the atoms due to the structural phase transition are shown in figure 4. To illustrate the idea more clearly, only part of a unit cell is displayed for clarity. The black arrows indicate the directions and amplitudes of the movement of each atom after crossing the 156 K phase transition towards low temperatures. The largest changes appear in the BO_3 triangles. They tilt away from the ab plane.

To further investigate the structural correlation with the magnetoelectric effect in $RX_3(BO_3)_4$, the atomic positions relative to $SmFe_3(BO_3)_4$ have been studied and are shown in figure 5 for data taken at 25 K. $SmFe_3(BO_3)_4$ is known to have the largest electric field-induced polarization at low temperature among the $RFe_3(BO_3)_4$ systems (R = Sm, Eu, Ho, Gd) and does not undergo a structural phase transition (maintains
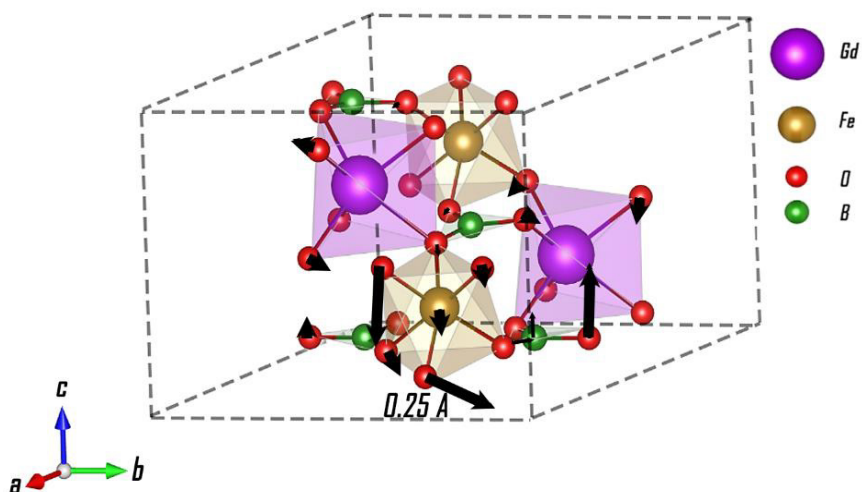
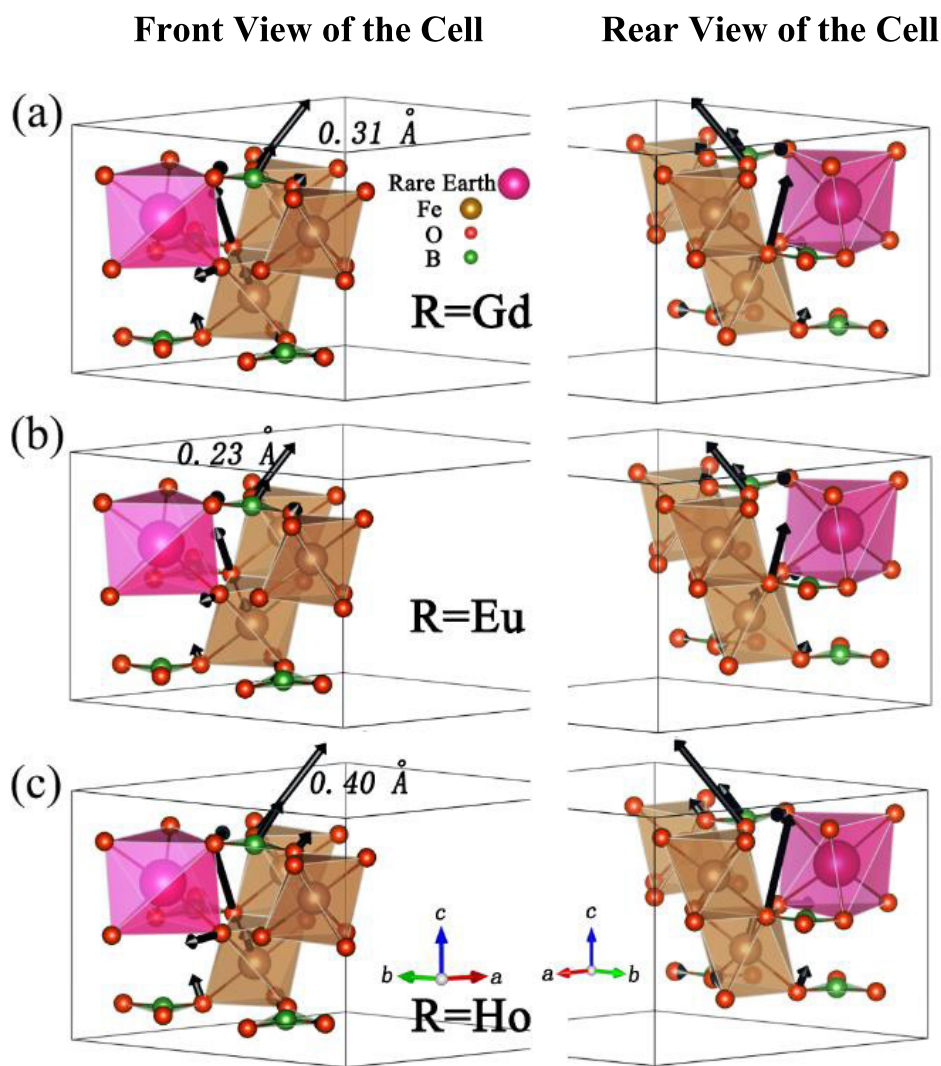**Figure 4.** Displacement of atoms on going from the from R32 (high temperature) to P3$_1$21 (low temperature) in GdFe$_3$(BO$_3$)$_4$.

Front View of the Cell   Rear View of the Cell

Figure 5. Relative atom displacements in the RFe$_3$(BO$_3$)$_4$ system with respect to SFBO at 25 K for (a) R = Gd, (b) Eu, (c) Ho, respectively. The data for Gd, Eu and Ho were taken at 25 K. In order to view the atoms which are displaced in the left hand column gives unit cells viewed from the front, while the rear view is given in the right column.

R32 space group). Thus, it is useful as a reference material. Refined structures at 25 K for GFBO, EFBO and HFBO are superposed on the structure of SFBO at 25 K to find the displacement of each atom site, respectively. Figure 5 thus shows the changes in structure at low temperature for GFBO (top), EFBO (middle) and HFBO (bottom) with respect to SFBO, for each case the front view (left) and rear view (right) of the structures are provided.

In figure 5, once again, the arrows reflect the amplitudes and directions of the displacement of specific atoms, and the numbers indicate the value of the largest change. For each structure, the arrows are to scale. In the systems with R = Gd, Eu, and Ho, the differences in the atomic positions are consistent: the largest change in each of the systems is the tilting of the BO_3 plane and the O_3 plane of the connected FeO_6 polyhedra (away from being parallel with the unit cell *a-b* plane). The displacement pattern is the same for all three samples shown in the figure. The tilting angles of the BO_3 with respect to the *ab* plane for R = Gd, Eu and Ho are 10.9°, 9.6°, 12.2°, respectively. From a structural perspective, it appears that the transition to the $P3_121$ space group is one of the major reasons for the dramatic decrease in the magnetoelectric effect for systems with R = Gd, Eu, and Ho.

As suggested in the literature (see for example review [1–5]), the BO_3 units function as ferroelectric-active groups mainly due to π electrons. In the case of $RX_3(BO_3)_4$, the symmetry-lowering tilting of the BO_3 and FeO_6 structural groups may greatly weaken the π bonding of the BO_3 as well as reduce the coupling between the ferroelectric active BO_3 groups and the magnetic groups RO_6 and FeO_6. We note that the largest electric-field-induced polarization of $RX_3(BO_3)_4$ lies in the *ab* plane. The motion described above might be one of the major reasons for the reduction of the magnetoelectric effect in the system. This is in good agreement with the published results that the electric field induced polarization of $HoFe_3(BO_3)_4$, $GdFe_3(BO_3)_4$ and $EuFe_3(BO_3)_4$ are much lower than systems like $SmFe_3(BO_3)_4$ and $NdFe_3(BO_3)_4$. Meanwhile, our previous research indicated that $HoAl_3(BO_3)_4$ is much stiffer along the *c* axis [29], which would result in much larger couplings between the ferroelectric and magnetic units as suggested by the above theory. In this system, the polyhedra and BO_3 planes are less likely to tilt. This is also supported by the experimental result [20] that the magnetoelectric effect in the $HoAl_3(BO_3)_4$ is greater than it is in the $SmFe_3(BO_3)_4$ by the factor of ~10.

We note that in the case of R = Gd [36], application of pressure results in an abrupt increase in the *a/c* ratio (near 25 GPa). This is opposite to what is observed as the temperature is reduced (see transition near ~156 K, figure 3(a)) to low temperatures in the region where magnetoelectric measurements. The major change with pressure in the R = Gd system is a sudden compression of the *c*-axis while the *a*-axis changes smoothly with a smaller slope [36]. We also note the significantly higher *a/c* ratio for the HABO system (compared to the RFBO systems) with large magnetoelectric effect. These combined results suggest that pressure (*c*-axis uniaxial pressure) may maintain the R32 structure (destabilizing the $P3_121$ phase) and possibly enhance magnetoelectric properties.
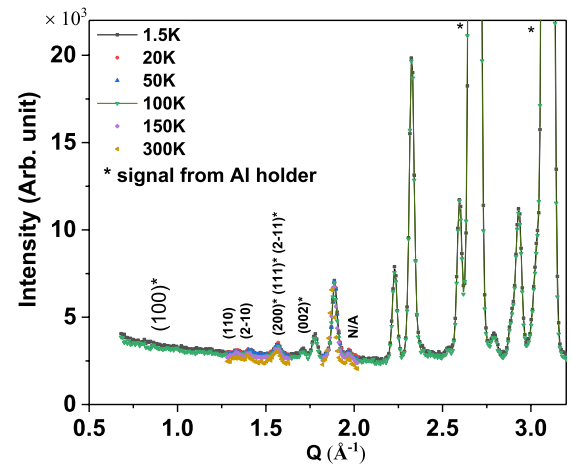
(a)
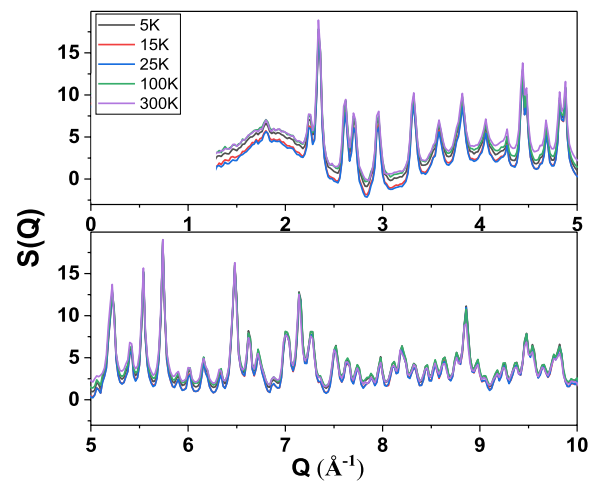
(b)

Figure 6. Powder neutron diffraction under ambient field taken from (a) HB-1 and (b) NOMAD for $HoAl_3(BO3)_4$.

To explore the possibility of low-temperature magnetic ordering on both R sites and Fe sites, neutron scattering measurements were conducted. Recent studies showed that the transition metal Fe is not essential to establish large magnetoelectricity in this class of materials [37]. At the same time, preliminary investigations [14] suggested possible Ho site ordering in $HoAl_3(BO_3)_4$ at low temperatures, due to the appearance of a signal at the calculated position of the (1 0 0) forbidden peak.

Powder and single-crystal neutron diffraction experiments were performed (figure 6). The powder diffraction measurements between 5 K and 300 K reveal no new peaks at low temperatures suggesting no long-range magnetic ordering at zero magnetic field. Zero field single-crystal diffraction measurements were conducted to enhance the signal to noise ratio and to examine the region around the (1 0 0) peak. Temperature-dependent pair distribution function (PDF) measurements on $HoAl_3(BO_3)_4$ were conducted at the NOMAD beamline at the Spallation Neutron Source (SNS), Oak Ridge National Laboratory (ORNL) and they are shown in figure 7. The local structure of HABO is seen to be stable with no obvious structural distortion with reduced temperature. This is consistent
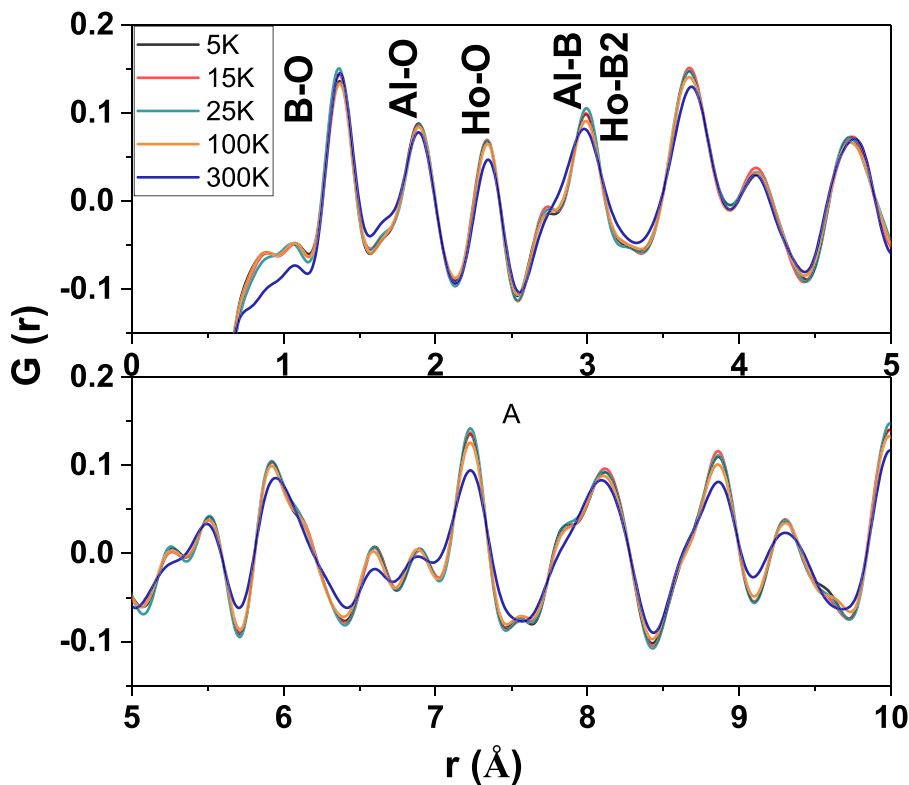
Figure 7. $G(r)$ profile of HABO between 5 K and 300 K under ambient magnetic field with the data taken at NOMAD beamline.
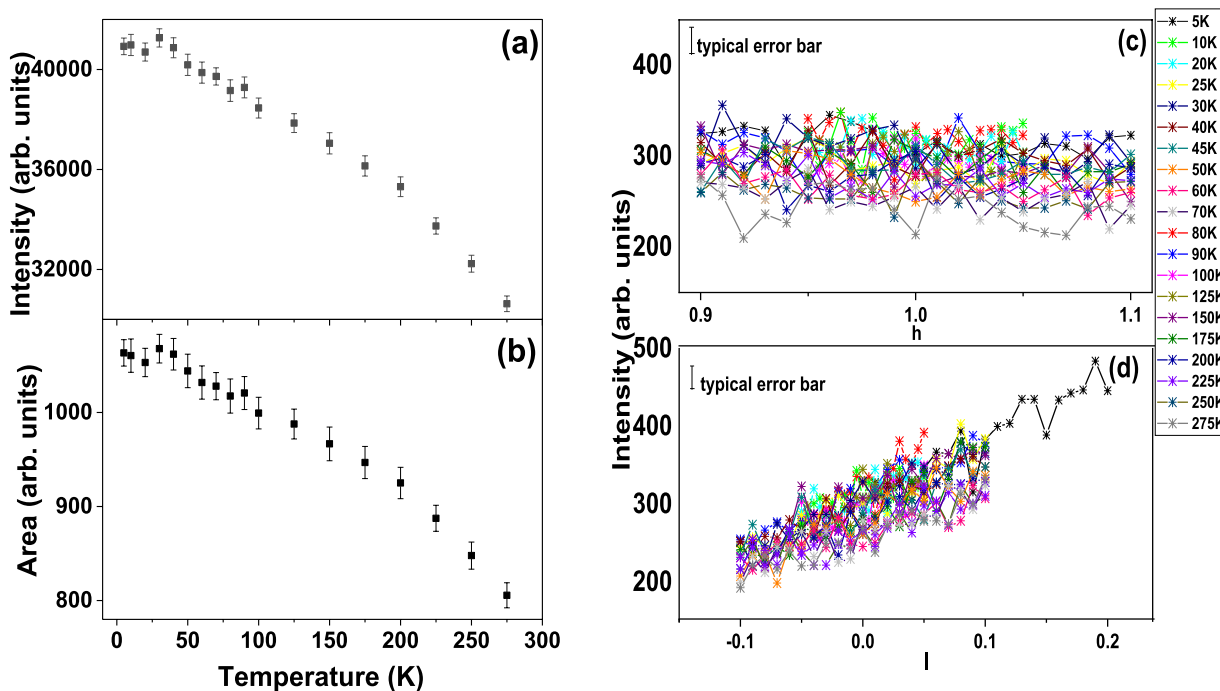

Figure 8. (a) Intensity and (b) area for $(2\,0\,2)$ peak versus temperature from single-crystal diffraction data on $HoAl_3(BO3)_4$. (c) Radial and (d) transverse scan of the region around the expected position of the peak $(1\,0\,0)$ for single crystal diffraction data on $HoAl_3(BO3)_4$.

with the long-range structural parameters derived from high and low-temperature single-crystal x-ray diffraction (supplementary document). Structural data at high and low temperatures are given in the tables and the supplementary document.

For the single crystal measurement, the crystal was first aligned with the *c* axis in the horizontal plane to find the $(2\,0\,2)$

and $(0\,0\,3)$ peak. The predicted position of the $(1\,0\,0)$ peak was then calculated and scanned along the radial and transverse directions between 5 K to 300 K. Single crystal measurements results are given in figure 8. Figures 8 gives (a) the height and (b) the area of the peak $(2\,0\,2)$ after fitting the experimental data with a Gaussian profile. No anomalies can be

seen through the entire temperature region. Figure 8(c) gives the radial and 8(d) the transverse scan of the region around the calculated position of the (1 0 0) forbidden peak. The data seem to be flat between 5 K and 300 K with no obvious appearance or disappearance of a peak. The results from our neutron scattering indicate no evidence of magnetic ordering in $HoAl_3(BO_3)_4$ perpendicular to the *a*-axis and no structural changes with reduced temperature.

With respect to magnetoelectric properties, the important ions are the rare earth ions. High-resolution single crystal x-ray diffraction measurements in magnetic field may reveal the exact motions of the R site ions leading to a quantitative microscopic model. This will be the subject of future work.

4. Conclusion

We have conducted single-crystal x-ray and neutron diffraction measurements between 5 K and 300 K on $RX_3(BO_3)_4$ (R = Ho, Eu, Sm, Nd, Gd; X = Fe, Al). The results suggest that the reduced coupling between ferroelectric and magnetic groups caused by the tilting of BO_3 planes and FeO_6 polyhedra may be the main reason for the dramatic decrease of the magnetoelectricity in systems with R = Ho, Eu, Gd, and X = Fe. No magnetic ordering perpendicular to the *a*-axis was detected in $HoAl_3(BO_3)_4$. We predict that the application of uniaxial pressure in $RFe_3(BO_3)_4$ may stabilize the high-temperature R32 phase and potentially enhance the magnetic field induced polarization.

Supporting information

IR spectrum for NFBO, double Debye model fits and single crystal structure refinement results of all the samples at the highest and the lowest temperature measured.

ORCID iDs

Y-S Chen ⬤ https://orcid.org/0000-0002-7646-7761
R P S M Lobo ⬤ https://orcid.org/0000-0003-2355-6856
T A Tyson ⬤ https://orcid.org/0000-0001-8646-1470

References

[1] Wu H, Li L, Liang L-Z, Liang S, Zhu Y-Y and Zhu X-H 2015 *J. Eur. Ceram. Soc.* **35** 411
[2] Johnson R D and Radaelli P G 2014 *Annu. Rev. Mater. Res.* **44** 269
[3] Spaldin N A, Cheong S W and Ramesh R 2010 *Phys. Today* **63** 38
[4] Wang K F, Liu J M and Ren Z F 2009 *Adv. Phys.* **58** 321
[5] Cheong S-W and Mostovoy M 2007 *Nat. Mater.* **6** 13
[6] Ramesh R and Spaldin N A 2007 *Nat. Mater.* **6** 21
[7] Kuzmenko A M *et al* 2018 *Phys. Rev. Lett.* **120** 027203
[8] Frolov K V *et al* 2018 *J. Alloys Compd.* **748** 989
[9] Kadomtseva A M *et al* 2018 *Phys. Rev.* B **89** 014418
[10] Vasiliev A N and Popova E A 2006 *Low Temp. Phys.* **32** 735
[11] Kadomtseva A M, Popov Yu F, Vorob'ev G P, Pyatakov A P, Krotov S S, Kamilov K I and Ivanov V Yu 2010 *Low Temp. Phys.* **36** 511
[12] Saeed Y, Singh N and Schwingenschlögl U 2011 *J. Appl. Phys.* **110** 103512
[13] Liang K C, Chaudhury R P, Lorenz B, Sun Y Y, Bezmaternykh L N, Temerov V L and Chu C W 2011 *Phys. Rev.* B **83** 180417
[14] Heitmann T, Zhang Q, Liang K C, Bezmaternykh L M, Temerov V L, Lorenz B and Vaknin D 2013 *Annual Fall Meeting of the APS Prairie Section, PSF13 Meeting of the American Physical Society*
Heitmann T private communications
[15] Zinenko V I, Pavlovskii M S, Krylov A S, Gudim I A and Eremin E V 2013 *J. Exp. Theor. Phys.* **117** 1032
[16] Kadomtseva A M, Zvezdin A K, Pyatakov A P, Kuvardin A V, Vorob'ev G P, Popov Y F and Bezmaternykh L N 2007 *J. Exp. Theor. Phys.* **105** 116
[17] Popov Y F, Pyatakov A P, Kadomtseva A M, Vorob'ev G P, Zvezdin A K, Mukhin A A, Ivanov V Y and Gudim I A 2010 *J. Exp. Theor. Phys.* **111** 199
[18] Kurumaji T, Ohgushi K and Tokura Y 2014 *Phys. Rev.* B **89** 195126
[19] Zvezdin A K, Vorob G P, Kadomtseva A M, Popov Y F, Bezmaternykh L N, Kuvardin A V and Popova E A 2006 *JETP Lett.* **83** 509
[20] Hinatsu Y, Doi Y, Ito K, Wakeshima M and Alemi A 2003 *J. Solid State Chem.* **172** 438
[21] Mo H, Nelson C S, Bezmaternykh L N and Temerov V T 2008 *Phys. Rev.* B **78** 214407

[22] Janoschek M, Fischer P, Schefer J, Roessli B, Pomjakushin V, Meven M, Petricek V, Petrakovskii G and Bezmaternikh L 2010 *Phys. Rev.* B **81** 094429

[23] Fischer P *et al* 2006 *J. Phys.: Condens. Matter* **18** 7975

[24] Ritter C, Pankrats A, Gudim I and Vorotynov A 2012 *J. Phys.: Condens. Matter* **24** 386002

[25] Ritter C, Vorotynov A, Pankrats A, Petrakovskii G, Temerov V, Gudim I and Szymczak R 2010 *J. Phys.: Condens. Matter* **22** 206002

[26] Ritter C, Vorotynov A, Pankrats A, Petrakovskii G, Temerov V, Gudim I and Szymczak R 2008 *J. Phys.: Condens. Matter* **20** 365209

[27] Ritter C, Balaev A, Vorotynov A, Petrakovskii G, Velikanov D, Temerov V and Gudim I 2007 *J. Phys.: Condens. Matter* **19** 196227

[28] Bezmaternykh L, Temerov V and Gudim I 2005 *Crystallogr. Rep.* **50** 97

[29] Zhang H, Yu T, Chen Z, Nelson C S, Bezmaternykh L N, Abeykoon A M M and Tyson T A 2015 *Phys. Rev.* B **92** 104108

[30] Hwang J S, Lin K J and Tien C 1997 *Rev. Sci. Instrum.* **68** 94

[31] Bruker X A P E 2009 *Saint and SADABS* (Madison, WI: Bruker AXS Inc.)

[32] Sheldrick G 2003 *XPREP* (Madison, WI: Bruker AXS Inc.)

[33] Sheldrick G 2015 *Acta Crystallogr.* A **71** 3

[34] Spek A 2003 *J. Appl. Crystallogr.* **36** 7

[35] Moreira R L, Lobo R P S M, Ramos S L, Sebastian M T, Matinaga F M, Righi A and Dias A 2018 *Phys. Rev. Mater.* **2** 054406

[36] Gavriliuk A, Kharlamova S A, Lyubutin I, Troyan I A, Ovchinnikov S, Potseluiko A, Eremets M and Boehler R 2004 *J. Exp. Theor. Phys. Lett.* **80** 426

[37] Chaudhury R P, Lorenz B, Sun Y Y, Bezmaternykh L N, Temerov V L and Chu C W 2010 *Phys. Rev.* B **81** 220402